Geophysical Research Letters

RESEARCH LETTER
10.1029/2018GL078378

Key Points:
- Mantle transition zone properties below the United States are determined by relating receiver function images to mineral physics-based seismic profiles
- Transition zone characteristics of the eastern United States are linked to Farallon subduction
- The top of the lower mantle beneath the southeastern United States is enriched in basalt

Supporting Information:
- Supporting Information S1

Correspondence to:
R. Maguire,
romaguir@umich.edu

Citation:
Maguire, R., Ritsema, R., & Goes, S. (2018). Evidence of subduction-related thermal and compositional heterogeneity below the United States from transition zone receiver functions. *Geophysical Research Letters*, *45*, 8913–8922. https://doi.org/10.1029/2018GL078378

Received 16 APR 2018
Accepted 1 AUG 2018
Accepted article online 9 AUG 2018
Published online 4 SEP 2018

Evidence of Subduction-Related Thermal and Compositional Heterogeneity Below the United States From Transition Zone Receiver Functions

Ross Maguire[1], Jeroen Ritsema[1], and Saskia Goes[2]

[1]Department of Earth and Environmental Sciences, University of Michigan, Ann Arbor, MI, USA, [2]Department of Earth Science and Engineering, Imperial College London, London, UK

Abstract The subduction of the Farallon Plate has altered the temperature and composition of the mantle transition zone (MTZ) beneath the United States. We investigate MTZ structure by mapping *P*-to-*S* conversions at mineralogical phase changes using USArray waveform data and theoretical seismic profiles based on experimental constraints of phase transition properties as a function of temperature and composition. The width of the MTZ varies by about 35 km over the study region, corresponding to a temperature variation of more than 300 K. The MTZ is coldest and thickest beneath the eastern United States where high shear velocity anomalies are tomographically resolved. We detect intermittent *P*-to-*S* conversions at depths of 520 km and 730 km. The conversions at 730-km depth are coherent beneath the southeastern United States and are consistent with basalt enrichment of about 50%, possibly due to the emplacement of a fragment of an oceanic plateau (i.e., the Hess conjugate).

Plain Language Summary The Earth's mantle transition zone between depths of about 400 km and 800 km is characterized by mineralogical phase transitions that depend on pressure, temperature, and composition. Seismic waves that propagate through mineral phase transitions can change polarization: a compressional wave (*P* wave) can change into a transverse wave (*S* wave). In this study, we analyze *P*-to-*S* converted waves using recordings of earthquakes from a network of seismographs in the United States (i.e., the USArray). From estimates of the arrival times and amplitudes of *P*-to-*S* conversions, we map the depths and strength of mineral phase transitions and the temperature and composition of the transition zone. Our seismic observations confirm models of the geologic history of Farallon Plate subduction along the western margin of the North American continent. The mantle transition zone is coolest beneath the eastern United States, and fragments of former oceanic plateaus are still present at the base of the transition zone beneath the Gulf of Mexico region.

1. Introduction

The subduction of oceanic lithosphere brings thermal and compositional heterogeneity into the mantle transition zone (MTZ). The transitions to denser mineral phases occur at different pressures in the different chemical components of the slab, including sediments, crust, and the depleted mantle lithosphere. Over geologic time, mechanical mixing may produce a compositional gradient across the MTZ since basaltic components accumulate preferentially above the 660-km phase transition and melt-depleted, harzburgitic components concentrate below it (e.g., Mambole & Fleitout, 2002; Nakagawa et al., 2010; Xie & Tackley, 2004). Large fragments of recently subducted slabs may still be intact and distributed within the MTZ.

North America is an ideal region for studying the structure of the MTZ and its modification by plate subduction in the Cenozoic and Mesozoic. Tomographic images of the mantle beneath North America (e.g., S. Burdick & Lekic, 2017; Grand, 1994; Porritt et al., 2014; Sigloch et al., 2008; Sigloch, 2012; Schmandt & Lin, 2014; van der Lee & Nolet, 1997) reveal high-velocity anomalies within or just below the MTZ beneath the central and eastern United States which may be relics of the Farallon oceanic plate. A phase of low-angle (i.e., flat-slab) subduction may explain the distribution of these slab remnants far from the ancient trench axis and the eastward propagation of deformation and arc-like magmatism during the Laramide orogeny (e.g., Coney & Reynolds, 1977; Humphreys et al., 2003). Livaccari et al. (1981) suggested that the subduction of an oceanic plateau may provide the necessary buoyancy since the thickened oceanic crust and depleted harzburgite

residue are less dense than the surrounding mantle. Liu et al. (2010) suggested that buoyancy forces from the conjugate halves of the Shatsky Rise and Hess Rise play a critical role in flat-slab subduction of the Farallon plate. They predicted that the subducted oceanic plateaus are presently located at the top of the lower mantle beneath the southeastern United States (the Hess conjugate) and to the east of the Great Lakes region (the Shatsky conjugate). H. Wang et al. (2017) suggested that the eclogitized Hess conjugate caused Laramide age subsidence in the Gulf of Mexico region.

The deployment of the USArray since 2004 has produced new seismic data for imaging the mantle with high spatial resolution. The USArray includes 120 Reference Network stations and about 400 Transportable Array stations with about 70-km station spacing. The TA stations were redeployed at sites in the western United States and the eastern United States between 2004 and 2013. Building on previous analyses, we develop receiver function images from USArray waveform data to map seismic discontinuities in the MTZ. Using mineral physics relationships between temperature, composition, and seismic velocity, we associate the discontinuities with mineral phase transitions and estimate variations in temperature and composition from their relative depths and strengths. In particular, we investigate whether fragments of relatively cold slabs and relatively dense oceanic plateaus at the base of the MTZ, are evident in receiver functions to corroborate previous tomographic and geodynamic observations.

2. Receiver Functions

2.1. Method

As is well documented (e.g., Deuss et al., 2013; Shearer, 2000), phase transitions in the olivine system produce sharp gradients in seismic velocity observed near depths of 410, 520, and 660 km. Additional seismic discontinuities have been observed near the base of the transition zone between about 660 and 750 km depth (e.g., Deuss et al., 2006; Simmons & Gurrola, 2000; X. Wang & Niu, 2011), which are commonly interpreted as phase transitions in the garnet system, although a poststishovite phase transition may be important in subduction settings (Tauzin et al., 2018). Since garnet is a primary constituent in basaltic material at transition zone pressures, the detection of seismic signals produced just below 660-km depth may provide a useful estimate of the basalt content at the base of the MTZ.

In this study, we use the *Pds* receiver function method (e.g., L. Burdick & Langston, 1977; Kind et al., 2012; Vinnik, 1977) to image seismic velocity gradients in the MTZ. The *Pds* phase is a *P*-to-*S* wave conversion at depth *d*. Its amplitude and arrival time depend on the impedance contrast and depth of the seismic discontinuities or velocity gradients associated with mineral phase transitions. We compute receiver functions by rotating the original seismograms into the RTZ coordinate system, filtering the waveforms with a band-pass filter between periods of 5 and 50 s, cutting waveform sections that begin 10 s before and end 120 s after the predicted *P* wave arrivals, and deconvolving the vertical from the radial component waveforms using the time domain matrix inversion method (e.g, Gurrola et al., 1995). The deconvolution is stabilized by using a damping parameter λ (we use $\lambda = 5$) to suppress noise without excessive low-pass filtering.

We analyze USArray recordings of all earthquakes which occurred between 2008 and 2014 and with moment magnitudes between 6 and 7 (supporting information, Figure S1). We include event-station pairs for epicentral distances between 30° and 90°. We cull receiver functions both visually and using the signal-to-noise criterion that the root-mean-square amplitude of a 5-s window centered on the *P* onset must be at least 3 times larger than the root-mean-square amplitude of a 20-s window (Schmandt et al., 2012). After quality control, roughly half of the data set has been rejected, retaining 46,026 high-quality receiver functions.

We migrate the receiver functions to depth using the common conversion point (CCP) technique (e.g., Dueker & Sheehan, 1997; Eagar et al., 2010; Gao & Liu, 2014; Schmandt et al., 2012). Voxels in the imaging domain are about 50×50-km^2 wide and 2-km thick. At a given depth, receiver function signals contribute to all points in the CCP volume which are within one Fresnel zone radius of the pierce point. The Fresnel zone radius is calculated for a 5-s period *S* wave. We estimate and subtract the contributions of 3-D velocity anomalies to the *Pds* and *P* traveltimes by ray tracing through the tomographic model US-SL-2014 (Schmandt & Lin, 2014) using the TauP method (Crotwell et al., 1999). The distribution of epicentral distances has a slight bias toward larger distances, and the majority of the events were in South America and the western Pacific (see supporting information Figure S1). In Figure S2, we demonstrate that the imaging artifacts due to the incomplete illumination geometry do not affect the main conclusions drawn from the analysis.

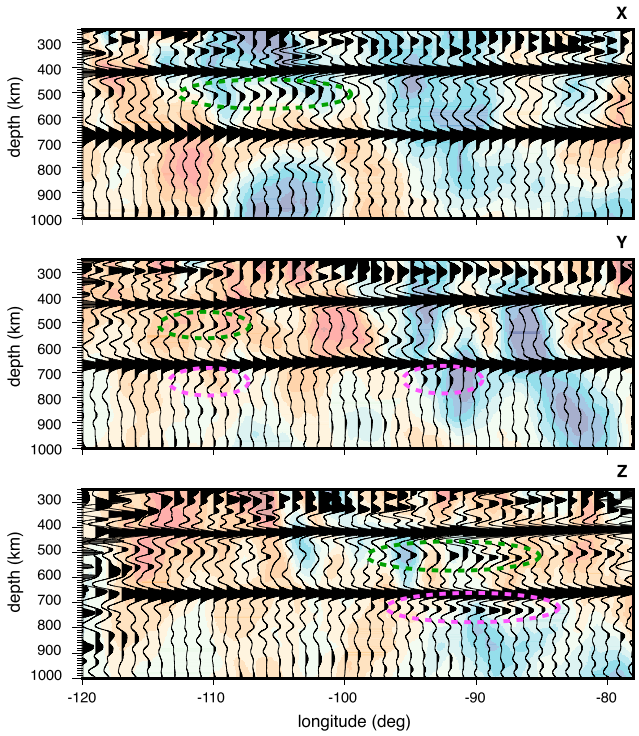

Figure 1. Longitudinal cross sections through the CCP imaging volume for (from top to bottom) latitude 44°N (profile X), 38°N (profile Y), and 32°N (profile Z). High-amplitude conversions from the 520 and 730 are indicated by green and pink circles, respectively. The background depicts the shear velocity structure of tomographic model US-SL-2014 (Schmandt & Lin, 2014). The locations of the cross sections are shown in Figure 4d.

2.2. CCP Cross Sections

Figure 1 shows vertical cross sections through the CCP image along parallels at latitudes 44°N (profile X), 38°N (profile Y) and 32°N (profile Z). The migrated receiver functions are superposed on the shear velocity structure of US-SL-2014 (Schmandt & Lin, 2014). *P*-to-*S* conversions from the 410- and 660-km discontinuities (i.e., *P*410*s* and *P*660*s*) are the largest phases and coherent throughout the CCP image. Their amplitudes vary, but on average they are both about 4% of the direct *P* arrival. Along each cross section, the depths of the 410 and 660 varies by as much as ±20 km. Regions with the strongest deflections of the 410 and 660 correspond to strong velocity anomalies in US-SL-2014. In general, regions with a positive velocity anomaly in the transition zone correspond to an anomalously thick MTZ, while the opposite is true for regions with a negative velocity anomaly.

Signals of conversions from near the 520 (i.e., *P*520*s*) are detected intermittently in each of the three cross sections (circled in green). In cross-section X, a strong 520 between −100° and −110° has an amplitude as large as 25% of *P*410*s* and corresponds to a high-velocity anomaly in US-SL2014. Weaker signals from 520 are present in cross-section Y in low-velocity regions. In cross-section Z, the 520 is apparent in several locations but shows no clear association with velocity anomalies. There is an apparent doubling of the 520 near the western end of cross-section Z, but the seismic data coverage is poor here and imaging artifacts may be substantial (see supporting information Figure S2).

Cross-section Z shows that a strong signal from the 730 is present between −85° and −95° (circled in pink). Here the maximum amplitude of *P*730*s* is about 30% of the amplitude of *P*660*s*. This signal coincides with a fast seismic velocity anomaly and a strong 520. Signals from 730 are also present in cross-section Y in a region of anomalously high seismic velocity, but with no associated detection of the 520.

The CCP images show complicated signals between 250- and 400-km depth, with single or double peaked arrivals coherent across broad regions. We do not interpret these signals since synthetic tests indicate the presence of artificial arrivals in this depth range (see supporting information S1). Negative velocity gradients above the 410 have been previously reported beneath the western United States (e.g., Hier-Majumder & Tauzin, 2017; Schmandt et al., 2011) which may be related to upper mantle melting. Sporadic and weak conversions are present between about 850-km and 1,000-km depth. Seismic layering in the lower mantle have been observed previously (e.g., Jenkins et al., 2017; Waszek et al., 2018), but there are no known mineral phase transitions that could account for these observations.

2.3. Phasing Diagrams

We verify that the observed *Pds* conversions from the 520 and 730 have the expected slownesses by a phasing analysis (e.g., Fee & Dueker, 2004) of receiver functions from regions with the strongest signals. Figure 2 compares the stack of all 46,026 receiver functions (Figure 2a) to stacks of receiver functions that sample the northern Rockies (Figure 2b) and the southeastern United States (Figure 2c). We estimate amplitude uncertainties by bootstrap resampling the receiver function stacks (Efron & Tibshirani, 1986).

The move-out corrected stack for the full data set (bottom left of Figure 2a) represents the average transition zone structure beneath the USArray. The *P*410*s* and *P*660*s* conversions at the 410 and 660 are the main signals and have the predicted *P*-to-*S* move-out. The *P*520*s* and *P*730*s* conversions are invisible, confirming that the 520 and 730 are not coherent boundaries beneath the USArray. The 520 is detected in the stacks of both subsets, but the 730 is visible only in the stack from the southeastern United States (Figure 2c). Both the 520 and 730 signals are above noise level according to bootstrap resampling analysis. The phasing analysis diagrams (right panels of Figures 2b and 2c) confirm that the signals at 55 s after P (i.e., 9.8 s after *P*410*s*) and 73 s after *P* (i.e., 5.5 s after *P*410*s*) have slownesses and traveltimes consistent with *P*520*s* and *P*730*s*. It is unlikely

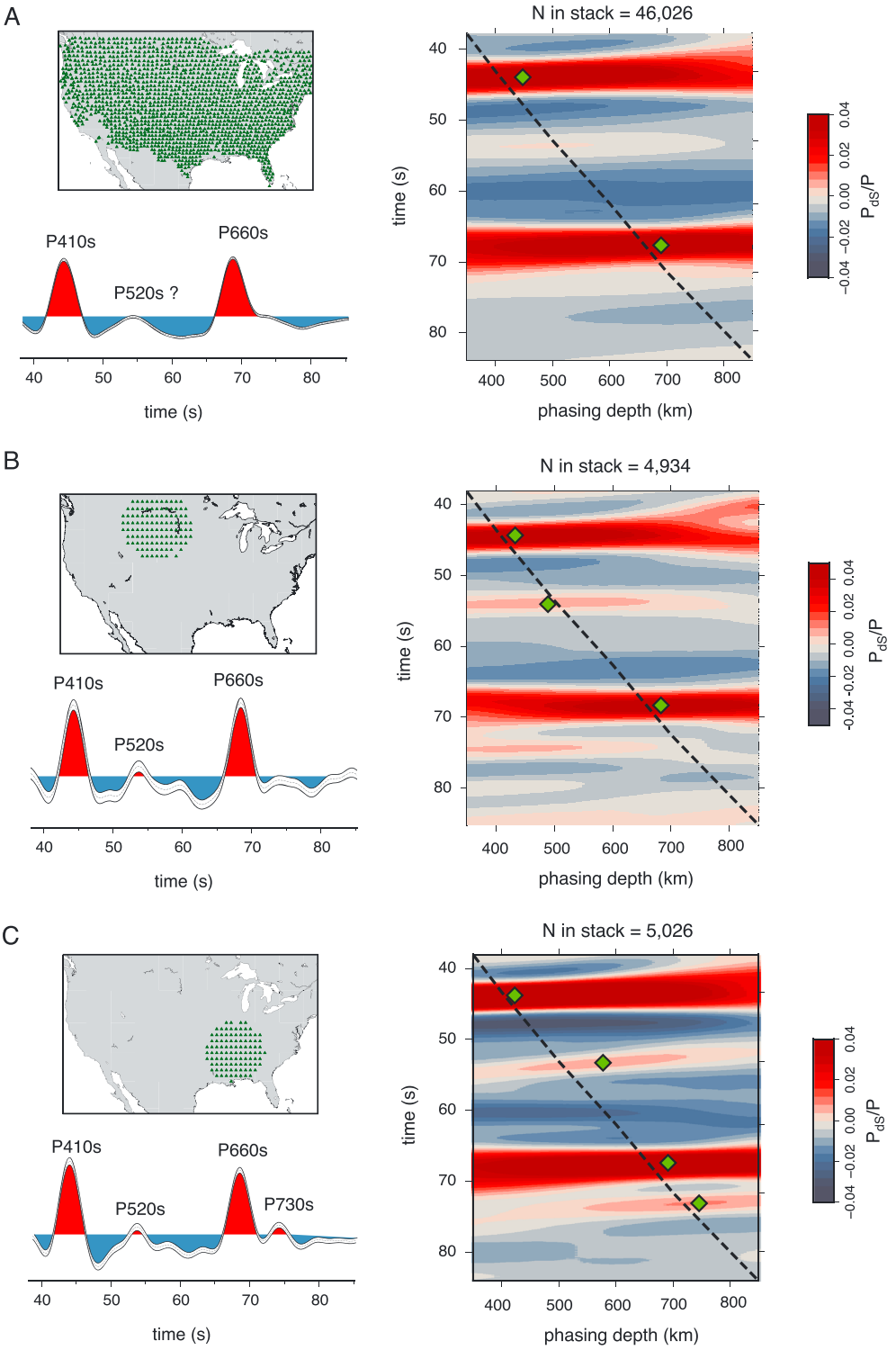

Figure 2. Comparison between receiver function stacks of the full data set (a), regional stacks of 4,934 receiver functions from stations in the northern Rockies (b), and 5,026 receiver functions from stations in the southeastern United States (c). Each region has three panels. The top left panel shows the included stations, the bottom left panel shows the move-out corrected stack, and the right panel shows a phasing analysis. The move-out corrected stacks show the average receiver function signal, as well as the upper and lower bound of the bootstrap confidence interval. Positively identified phases are labeled. Green diamonds shown in the phasing analysis indicate a local maximum.

that these signals are crustal shear wave reverberations following *P*410*s* and *P*660*s* since reverberations arrive with the same time delay after *P*410*s* and *P*660*s* (see supporting information Figure S3).

3. Interpretation

3.1. Modeling Temperature and Composition Dependent Velocity

We interpret our receiver function images of the transition zone using mineral physics modeling of the relationship between temperature, composition, and seismic velocity in the mantle. We compute the effects of temperature and composition on mineral phase equilibria and seismic velocities in the MTZ using the thermodynamic code Perple_X (Connolly, 2005) and the elastic parameter database of Stixrude and Lithgow-Bertelloni (2011). To account for the pressure- and temperature-dependent effects of anelasticity on seismic velocity, we correct the anharmonic velocity using the attenuation model Q7g (e.g., Maguire et al., 2016). We consider the mantle to be a mechanical mixture of basalt (i.e., recycled oceanic crust) and harzburgite (i.e., the melt-depleted fraction of oceanic lithosphere), which is a valid approximation if the reequilibration rate of basalt and harzburgite is slow compared to the convective time scale (Xu et al., 2008). We refer to the end member compositions basalt and harzburgite for simplicity, but the actual mineral assemblages depend on thermodynamic conditions. The relative fractions of basalt and harzburgite are defined as f and $1 - f$. We use the mid-ocean ridge basalt composition from Workman and Hart (2005) and harzburgite composition from Baker and Beckett (1999).

Figure 3a shows how the shear wave velocity V_S depends on the basalt fraction f in the mantle. Profiles of the *P* wave velocity have a similar character. Each profile of V_S is computed along an adiabat with a potential temperature of 1300 K. There are seismic discontinuities or sharp gradients near 300-, 410-, 520-, 660-, and 730-km depth. For a pyrolitic (i.e., $f \approx 0.2$) or harzburgite-enriched mantle ($f < 0.2$), the 410, 520, and 660 in the olivine system are dominant. Both the 410 and 660 are narrower than 10 km, and they are the largest discontinuities with shear velocity jumps of 7.5% and 7.2%, respectively. The 300 and 520 are weaker, and the 520 is spread over a broad depth interval.

As f increases, the 410, 520, and 660 phase changes in the olivine system weaken while the coesite to stishovite transformation near 300-km depth and the majorite garnet to bridgmanite transformation near 730 km depth become stronger. Low wave speeds throughout the transition zone also characterize a mantle enriched in basalt. The increase of V_S at the 730 is 1.8% for $f = 0.2$ and 11.1% for $f = 1$. The 730 is the only phase transition that occurs near the base of the transition zone in a purely basaltic mantle (when $f = 1$). Since the strength of the 660 and 730 depends strongly on f, we use the relative amplitudes of *P*660*s* and *P*730*s* to estimate the basalt fraction f. Figure 3b shows amplitude ratios from synthetic receiver functions computed for shear velocity profiles with variable f (see also supporting information Figure S4).

Figure 3c shows how phase changes and V_S in the upper mantle depend on temperature. Here we assume a homogeneous mantle composition with $f = 0.2$ (i.e., a roughly pyrolitic mantle). We vary the potential temperature of the adiabat between 1000 K and 2000 K, which is within about −600 K to +400 K of the average potential temperature of mid-ocean-ridge basalt suggested by Herzberg et al. (2007). Since the Clapeyron slope of the 410 and the 660 are +2.7 MPa/K and −1.3 MPa/K, respectively, the phase boundary topography of the 660 is much more subdued than the 410 for the same thermal anomaly, and the transition zone thickness varies from 200 to 325 km for our range of potential temperatures (Figure 3d).

In our modeling, the 730 is a strongly temperature-dependent exothermic transition with a Clapeyron slope of +5.6 MPa/K. Its depth varies between about 700 km (for the 1000 K adiabat) to greater than 850 km (for the 2000 K adiabat). In principle, the observed depth of the postgarnet transition could constrain temperature at the top of the lower mantle. However, the experimentally determined Clapeyron slope is highly uncertain, with reported values ranging from +0.8 MPa/K (Hirose et al., 1999) to +6.4 MPa/K (Oguri et al., 2000). Additionally, *P*730*s* is generally too weak in our data for it to be useful to map the temperature structure throughout the study region.

3.2. Transition Zone Properties

Our estimates of the MTZ thickness and temperature inferred from our mineral physics models are shown in Figure 4a. The thickness of the transition zone is on average 249 km with peak-to-peak variations of about 35 km. This is in good agreement with the study by Gao and Liu (2014). The variation in thickness is similar to the velocity variations at 400-km depth imaged in US-SL-2014 (Figure 4d) and implies that the temperature in the MTZ beneath the United States varies by more than 300 K. Estimates of transition zone thickness

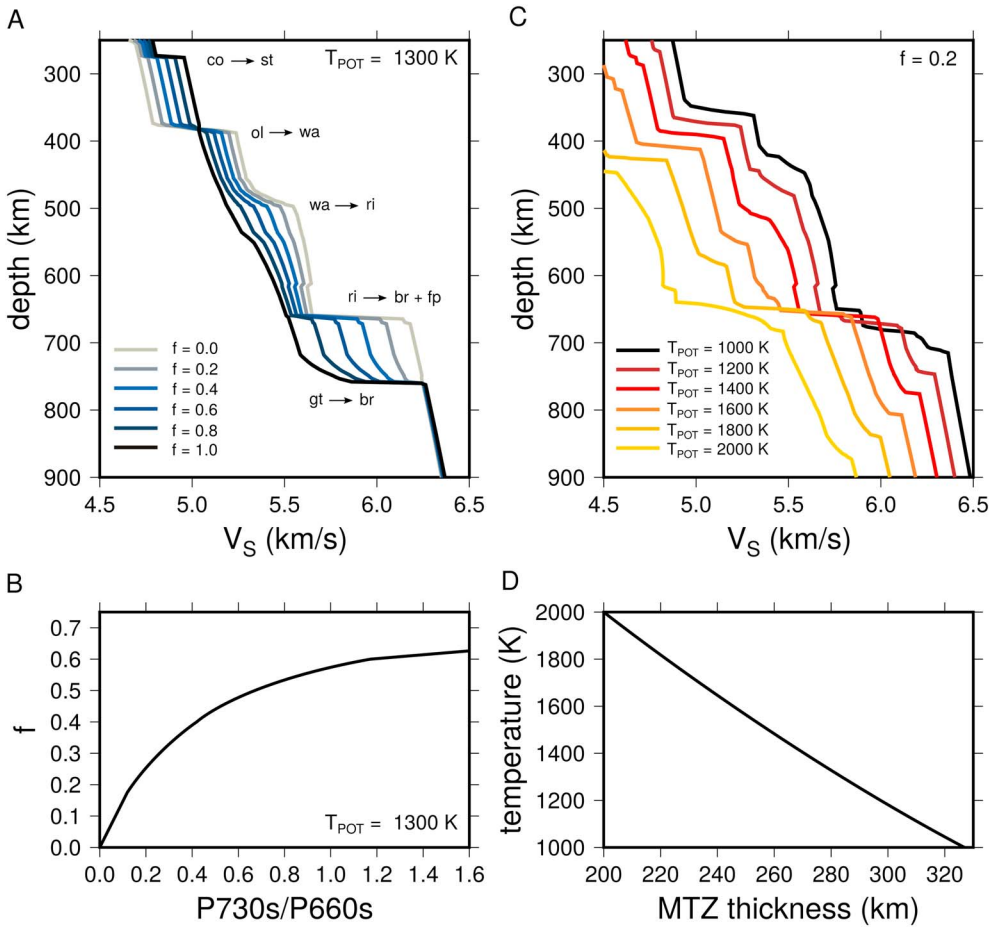

Figure 3. (a) Profiles of the shear velocity (V_S) for mechanical mixtures of harzburgite and mid-ocean-ridge basalt (MORB) as a function of MORB fraction *f* along a 1300 K adiabat. (b) Synthetic amplitude ratios of *P*730*s*/*P*660*s* for variable *f* (See supporting information). (c) V_S profiles for varying potential temperatures with a fixed MORB fraction of $f = 0.2$. (d) Mantle transition zone thickness for varying temperature. Mineral phase names in (a) and (c) are as follows: coesite (*co*), stishovite (*st*), olivine (*ol*), wadsleyite (*wa*), ringwoodite (*ri*), brigmanite (*br*), ferropericlase (*fp*), majorite garnet (*gt*). The 300, 410, 520, 660, and 730 correspond to the *co* → *st*, *ol* → *wa*, *wa* → *ri*, *ri* → *br* + *fp*, and *gt* → *br* mineral transitions, respectively.

and temperature change slightly depending on the seismic velocity model used to migrate receiver functions, but the general interpretations are robust (see supporting information Figure S5).

The transition zone is thinnest and therefore warmest beneath the western United States, except for the Columbia Plateau region to the east of the Cascades. This likely reflects the cooling of the mantle by the Juan de Fuca slab, which has penetrated into the MTZ although US-SL-2014 does not provide clear tomographic evidence for a high-velocity anomaly in the MTZ beneath this region. Yellowstone stands out as a small-scale region with an anomalously thin (230–240 km) transition zone, corresponding to a potential temperature of 1650–1750 K. It implies a deep origin of the Yellowstone hot spot, in agreement with Schmandt et al. (2012) and Tauzin et al. (2013) but not with Gao and Liu (2014), who do not find evidence for a thin transition zone beneath Yellowstone. The transition zone is relatively thick (260–270 km) over broad regions beneath the central and southeastern United States with maxima that coincide with high-velocity anomalies in US-SL-2014. We infer the potential temperature in these regions to be between 1400 and 1500 K.

Figure 4b shows the regions where 520 discontinuity appears to be the strongest. The amplitude of *P*520*s* is difficult to measure due to interference with the relatively strong side lobes of *P*410*s* and *P*660*s*, which are artifacts of waveform deconvolution. Therefore, we simply show in Figure 4b the regions where *P*520*s* is at least 20% of *P*410*s*, which we consider to be robust detections. The 520 is strong in the MTZ beneath the Columbia Plateau and northern Basin and Range, where we also resolve the transition zone to be relatively

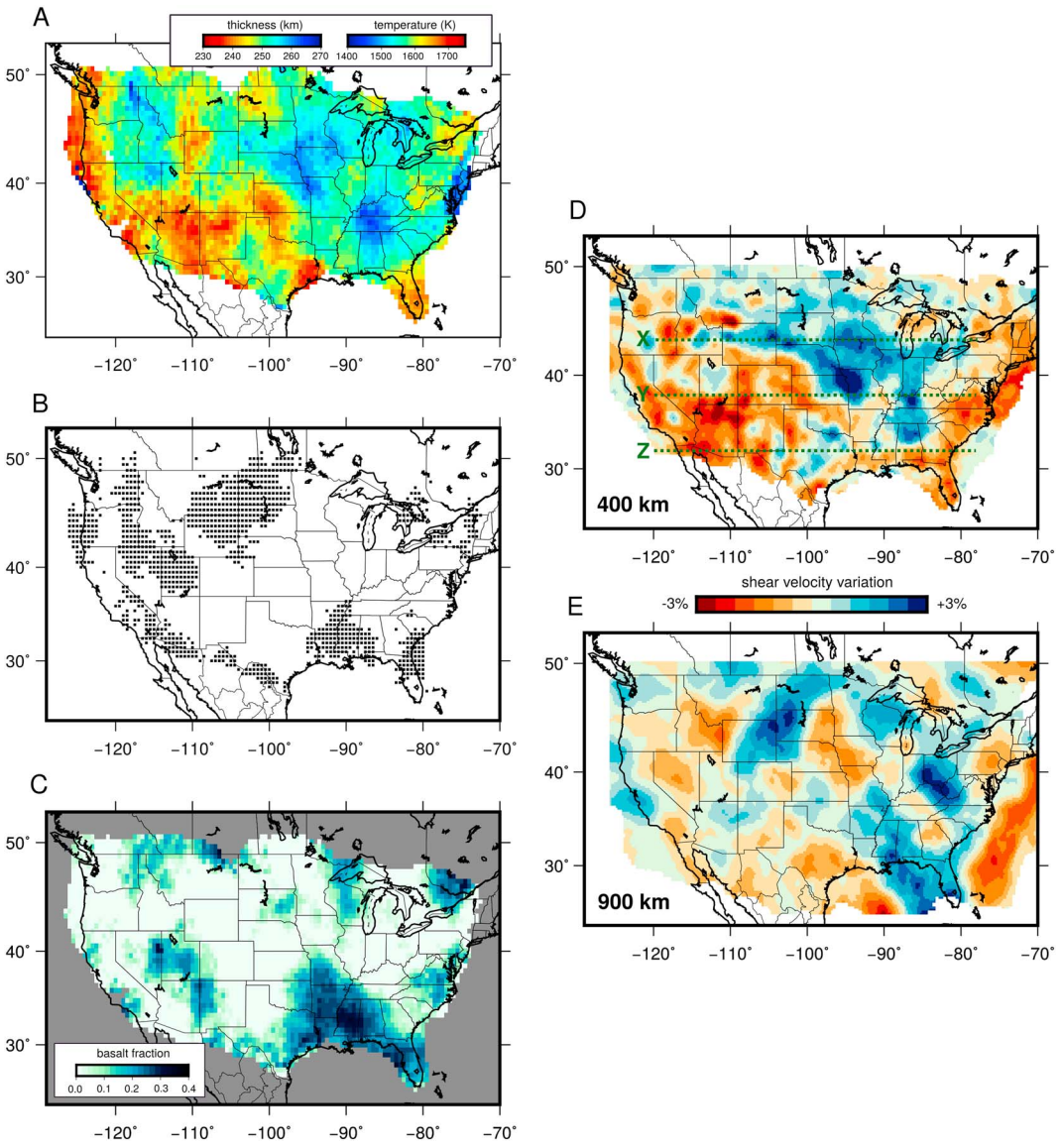

Figure 4. The maps on the left show (a) the thickness of the transition zone from *P*660*s*to*P*410*s* arrival times and the potential temperature as inferred from predicted seismic velocity profiles of MM pyrolite, (b) regions where *P*520*s* is detected with an amplitude of at least 20% of *P*410*s*, and (c) the inferred basalt fraction based on the *P*730*s* / *P*660*s* amplitude ratio. The maps on the right show shear velocity variations at depths of 400 km (d) and 900 km (e) according to model US-SL-2014. The dashed lines in (d) indicate the transects X, Y, and Z of the common conversion point cross sections shown in Figure 1.

thick and therefore cold. Further, we detect the 520 coherently over a broad area beneath the northern Great Plains and Rocky Mountain region where wave speeds are relatively high according to US-SL-2104. However, we do not find evidence for a cool and thick transition zone in this region, which would be expected if slabs of subducted material are present. The 520 is also apparent in the southeastern United States near the Gulf of Mexico. Here the thick transition zone and the high wave speeds provide complementary evidence for a cold downwelling.

Mineral physics models (Figure 3a) indicate that the impedance contrast at 520 increases with decreasing *f*. Therefore, Figure 4b may indicate regions of harzburgite enrichment. The absence of a pervasive detection of a 520 across the study area could indicate that the MTZ is enriched in basalt on average. It is also possible that the intermittent detection of the 520 may signify a local sharpening of the seismic discontinuity, rather than an increased impedance contrast, which would increase the seismic visibility. Recently, Mrosko et al. (2015)

found that the presence of water in transition zone under oxidizing environment reduces the stability field over which ringwoodite and wadsleyite coexist, and thus reducing the width of the 520 discontinuity. These conditions are expected in regions of subduction, and thus may explain the association we observe between detections of the 520 and inferred downwellings, particularly in the southeastern United States. A hydrated transition zone beneath the Gulf of Mexico region has also been suggested by Courtier and Revenaugh (2013), who observe a strong 520 using multiple reverberations of *ScS*.

Figure 4c shows the variable basalt fraction f at the base of the MTZ inferred from amplitude ratios of *P*730*s* and *P*660*s*. We assume that $f = 0$ in regions where *P*730*s* is undetected, which may be inaccurate if *P*730*s* is masked by side lobes of adjacent arrivals, or if signals stack incoherently due to unmodeled 3-D velocity structure. Additionally, regions with negative arrivals below 660, for example, due to dehydration melting (e.g., Schmandt et al.,2014), would map as regions with $f = 0$. Nonetheless, Figure 4c reveals an intriguing pattern of the basalt content at the base of the transition zone.

The inferred basalt enrichment, with values $f > 0.3$, is highest in the southeastern United States near the Gulf of Mexico. This coincides with a region of thick transition zone and a detection of the 520. Additionally, US-SL-2014 maps a high-velocity anomaly at the top of the lower mantle in this region (Figure 4e). A similarly enriched mantle is found along the Atlantic coast to the east of the Appalachians with no concurrent detection of the 520. Small regions of enriched mantle are also found to the east of the Great Lakes region and near Lake Superior. The western United States is largely depleted with the exception of the Colorado Plateau region, with $f \approx 0.2$, and an east-west trending region north of Rockies with $f \approx 0.3$. The Northern Rockies region is also associated with a strong 520.

4. Discussion

In a pyrolitic mantle, the 520 and 730 should produce observable *P*520*s* and *P*730*s* wave conversions (see supporting information Figure S4), yet these signals are recorded intermittently. The low amplitudes of *P*520*s* and *P*730*s* may indicate a strongly compositionally layered mantle with basalt enrichment and depletion above and below the 660, respectively (e.g., Nakagawa et al., 2010). The 520 and 730 are weak or even absent in such a mantle. Our stack of the full set of receiver functions from all stations of the USArray is consistent with the geodynamic predictions of a compositional gradient in the MTZ beneath North America.

The local detections of *P*520*s* and *P*730*s* may indicate regions of the MTZ where a compositional gradient has been perturbed by vertical flow, either by sinking slabs or the ascent of plumes. In general, there is no clear correlation between the strength of the 520 and 730 discontinuities and the inferred MTZ temperature, although some trends are apparent.

1. The detection of the 520 typically coincides with high-velocity anomalies in US-SL-2014 within the MTZ, with a thick transition zone, or both.
2. The MTZ is coolest and the basalt enrichment is highest beneath the eastern United States.
3. Basalt enrichment in the Gulf of Mexico region correlates with a high-velocity anomaly, a detection of the 520, and a thick transition zone.

These results are consistent with a mantle that has been perturbed by recent subduction and with the widespread distribution of fragments of cold slabs in the MTZ beneath the eastern United States. Previous studies have interpreted the high-velocity anomalies in the MTZ as remnants of the Farallon slab, which subducted eastward from the western margin of the United States during the Mesozoic and Cenozoic (e.g., Bunge & Grand, 2000), although other subduction histories remain possible (e.g., Sigloch & Mihalynuk, 2013).

Geodynamic simulations by Liu et al. (2010) suggest that buoyancy forces from the conjugate halves of the Shatsky Rise and Hess Rise play a critical role in flat-slab subduction of the Farallon plate. Furthermore, they predicted that the subducted oceanic plateaus are presently located at the top of the lower mantle beneath the southeastern United States (the Hess conjugate) and to the east of the Great Lakes (the Shatsky conjugate). H. Wang et al. (2017) suggested that the negative buoyancy from the eclogitized Hess conjugate explains Laramide age subsidence in the Gulf of Mexico region. The presence of a subducted oceanic plateau (i.e., the Hess conjugate) may explain the strong signature of basalt enrichment that we observe beneath the southeastern United States.

5. Conclusions

CCP images (Figures 1 and 4) of receiver functions from 7 years of USArray waveform data indicate the variable strength of phase transitions in the transition zone. This is compatible with a mantle with basalt enrichment in the MTZ above the 660 and harzburgite enrichment in the mantle below the 660. The images, with a lateral resolution of about 100 km, indicate that the 410 and 660 transitions are the only coherent boundaries. The width between the 410 and 660 varies by about 35 km, consistent with temperature variations of 300 K. The lateral variations of the apparent transition zone thickness correlate with the wave speed variation resolved by tomography. The transition zone is relatively thick and cool beneath the eastern United States, due to the presence of fragments of the subducted Farallon slab.

The receiver functions include a strong *P* wave to *S* wave conversion from a depth of about 730 km beneath the Gulf of Mexico region, which is consistent with the garnet to bridgmanite phase transition within a relatively cold (1400–1500 K) slab fragment. The location of the reflector at 730-km depth correlates with the location of the subducted Hess conjugate predicted by geodynamic simulations (Liu et al., 2010). Our results demonstrate the potential of using the regional variability of the transition zone structure below 660-km depth to map compositional heterogeneity at the base of the transition zone.

Acknowledgments
All seismic data used in this study are available online through the IRIS data service (http://ds.iris.edu/ds/). This research has been funded by NSF grant EAR-1565511 to J. R., and NERC project NE/J008028/1 to S. G. R. M. acknowledges support from Turner Research Funds and the Rackham Graduate School at UM. The authors thank Benoit Tauzin and Stephen Gao for constructive reviews that improved this study.

References

Baker, M. B., & Beckett, J. R. (1999). The origin of abyssal peridotites: A reinterpretation of constraints based on primary bulk compositions. *Earth and Planetary Science Letters*, *171*(1), 49–61. https://doi.org/10.1016/S0012-821X(99)00130-2

Bunge, H. P., & Grand, S. P. (2000). Mesozoic plate-motion history below the northeast Pacific Ocean from seismic images of the subducted farallon slab. *Nature*, *405*(6784), 337.

Burdick, L. J., & Langston, C. a. (1977). Modeling crustal structure through the use of converted phases in teleseismic body-wave forms. *Bulletin of the Seismological Society of America*, *67*(3), 677–691.

Burdick, S., & Lekić, V. (2017). Velocity variations and uncertainty from transdimensional *P*-wave tomography of North America. *Geophysical Journal International*, *209*(2), 1337–1351. https://doi.org/10.1093/gji/ggx091

Coney, P. J., & Reynolds, S. J. (1977). Cordilleran Benioff zones. *Nature*, *270*, 403–406. https://doi.org/10.1038/275464a0

Connolly, J. a. D. (2005). Computation of phase equilibria by linear programming: A tool for geodynamic modeling and its application to subduction zone decarbonation. *Earth and Planetary Science Letters*, *236*(1-2), 524–541. https://doi.org/10.1016/j.epsl.2005.04.033

Courtier, A. M., & Revenaugh, J. (2013). A water-rich transition zone beneath the Eastern United States and Gulf of Mexico from multiple ScS reverberations. In S. D. Jacobsen & S. Van Der Lee (Eds.), *Earth's deep water cycle*. https://doi.org/10.1029/168GM14

Crotwell, H. P., Owens, T. J., & Ritsema, J. (1999). The TauP Toolkit: Flexible seismic travel-time and ray-path utilities. *Seismological Research Letters*, *70*, 154–160.

Deuss, A., Andrews, J., & Day, E. (2013). Seismic observations of mantle discontinuities and their mineralogical and dynamical interpretation, (1st ed.). In S. I. Karato (Ed.), *Physics and Chemistry of the Deep Earth*. Chichester, West Sussex, UK: Wiley and Sons Ltd.

Deuss, A., Redfern, S. A. T., Chambers, K., & Woodhouse, J. H. (2006). The nature of the 660-kilometer discontinuity in Earth's mantle from global seismic observations of PP precursors. *Science*, *311*(5758), 198–201. https://doi.org/10.1126/science.1120020

Dueker, K. G., & Sheehan, A. F. (1997). Mantle discontinuity structure from midpoint stacks of converted *P* to *S* waves across the Yellowstone hotspot track. *Journal of Geophysical Research*, *102*(B4), 8313. https://doi.org/10.1029/96JB03857

Eagar, K. C., Fouch, M. J., & James, D. E. (2010). Receiver function imaging of upper mantle complexity beneath the Pacific Northwest, United States. *Earth and Planetary Science Letters*, *297*(1-2), 141–153. https://doi.org/10.1016/j.epsl.2010.06.015

Efron, B., & Tibshirani, R. (1986). Bootstrap methods for standard error, confidence intervals, and other measures of statistical accuracy. *Statistical Science*, *1*(1), 54–75. https://doi.org/10.1214/ss/1177013817

Ekström, G., Nettles, M., & Dziewoński, A. M. (2012). The global CMT project 2004–2010: Centroid-moment tensors. *Physics of the Earth and Planetary Interiors*, *201*, 1–9. https://doi.org/10.1016/j.pepi.2012.04.002

Fee, D., & Dueker, K. (2004). Mantle transition zone topography and structure beneath the Yellowstone hotspot. *Geophysical Research Letters*, *31*, L18603. https://doi.org/10.1029/2004GL020636

Gao, S. S., & Liu, K. H. (2014). Mantle transition zone discontinuities beneath the contiguous United States. *Journal of Geophysical Research: Solid Earth*, *119*, 6452–6468. https://doi.org/10.1002/2014JB011253

Grand, S. P. (1994). Mantle shear structure beneath the Americas and surrounding oceans. *Journal of Geophysical Research*, *99*(B6), 11,591–11,621. https://doi.org/10.1029/94JB00042

Gurrola, H., Baker, G., & Minister, J. (1995). Simultaneous time-domain deconvolution with application to the computation of receiver functions. *Geophysical Journal International*, *120*, 537–543.

Herzberg, C., Asimow, P. D., Arndt, N., Niu, Y., Lesher, C. M., Fitton, J. G., et al. (2007). Temperatures in ambient mantle and plumes: Constraints from basalts, picrites, and komatiites. *Geochemistry, Geophysics, Geosystems*, *8*(2), Q02006. https://doi.org/10.1029/2006GC001390

Hier-Majumder, S., & Tauzin, B. (2017). Pervasive upper mantle melting beneath the western US. *Earth and Planetary Science Letters*, *463*, 25–35. https://doi.org/10.1016/j.epsl.2016.12.041

Hirose, K., Fei, Y., Ma, Y., & Mao, H. K. (1999). The fate of subducted basaltic crust in the Earth's lower mantle. *Nature*, *397*(6714), 53–56. https://doi.org/10.1038/16225

Humphreys, E., Hessler, E., Dueker, K., Farmer, G. L., Erslev, E., & Atwater, T. (2003). How Laramide-age hydration of north American lithosphere by the farallon slab controlled subsequent activity in the western United States. *International Geology Review*, *45*(7), 575–595. https://doi.org/10.2747/0020-6814.45.7.575

Jenkins, J., Deuss, A., & Cottaar, S. (2017). Converted phases from sharp 1000 km depth mid-mantle heterogeneity beneath Western Europe. *Earth and Planetary Science Letters*, *459*, 196–207. https://doi.org/10.1016/j.epsl.2016.11.031

Kind, R., Yuan, X., & Kumar, P. (2012). Seismic receiver functions and the lithosphere-asthenosphere boundary. *Tectonophysics*, *536-537*, 25–43. https://doi.org/10.1016/j.tecto.2012.03.005

Laske, G., Masters, G., & Reif, C. (2001). CRUST 2.0: A new global crustal model at 2x2 degrees. Institute of Geophysics and Planetary Physics, the University of California, San Diego. Retrieved from http://mahi. ucsd. edu/Gabi/rem. dir/crust/crust2.html

Lekić, V., & Fischer, K. M. (2017). Interpreting spatially stacked Sp receiver functions. *Geophysical Journal International*, *210*(2), 874–886. https://doi.org/10.1093/gji/ggx206

Liu, L., Gurnis, M., Seton, M., Saleeby, J., Müller, R. D., & Jackson, J. M. (2010). The role of oceanic plateau subduction in the Laramide orogeny. *Nature Geoscience*, *3*(5), 353–357. https://doi.org/10.1038/ngeo829

Livaccari, R. F., Burke, K., & Sengör, A. M. C. (1981). Was the Laramide orogeny related to subduction of an oceanic plateau? *Nature*, *289*, 276–278. https://doi.org/10.1038/289276a0

Maguire, R., Ritsema, J., van Keken, P. E., Fichtner, A., & Goes, S. (2016). *P*- and *S*-wave delays caused by thermal plumes. *Geophysical Journal International*, *206*(2), 1169–1178. https://doi.org/10.1093/gji/ggw187

Mambole, A., & Fleitout, L. (2002). Petrological layering induced by an endothermic phase transition in the Earth's mantle. *Geophysical Research Letters*, *29*(22), 2044. https://doi.org/10.1029/2002GL014674

Montagner, J. P., & Kennett, B. L. N. (1996). How to reconcile body-wave and normal-mode reference earth models. *Geophysical Journal International*, *125*(1), 229–248. https://doi.org/10.1111/j.1365-246X.1996.tb06548.x

Mrosko, M., Koch-Müller, M., McCammon, C., Rhede, D., Smyth, J. R., & Wirth, R. (2015). Water, iron, redox environment: Effects on the wadsleyite–ringwoodite phase transition. *Contributions to Mineralogy and Petrology*, *170*(1), 1–12. https://doi.org/10.1007/s00410-015-1163-2

Nakagawa, T., Tackley, P. J., Deschamps, F., & Connolly, J. A. D. (2010). The influence of MORB and harzburgite composition on thermo-chemical mantle convection in a 3-D spherical shell with self-consistently calculated mineral physics. *Earth and Planetary Science Letters*, *296*(3-4), 403–412. https://doi.org/10.1016/j.epsl.2010.05.026

Nissen-meyer, T., Van Driel, M., Stähler, S. C., Hosseini, K., Hempel, S., Auer, L., et al. (2014). AxiSEM: Broadband 3-D seismic wavefields in axisymmetric media. *Solid Earth*, *5*(1), 425–445. https://doi.org/10.5194/se-5-425-2014

Oguri, K, Funamori, N., Uchida, T., Miyajima, N., Yagi, T., & Fujino, K. (2000). Post-garnet transition in a natural pyrope: A multi-anvil study based on in situ X-ray diffraction and transmission electron microscopy. *Physics of Earth and Planetary Interiors*, *122*, 175–186. https://doi.org/10.1016/S0031-9201(00)00178-3

Porritt, R. W., Allen, R. M., & Pollitz, F. F. (2014). Seismic imaging east of the Rocky Mountains with USArray. *Earth and Planetary Science Letters*, *402*(C), 16–25. https://doi.org/10.1016/j.epsl.2013.10.034

Schmandt, B., Dueker, K. G., Hansen, S. M., Jasbinsek, J. J., & Zhang, Z. (2011). A sporadic low-velocity layer atop the Western U.S. mantle transition zone and short-wavelength variations in transition zone discontinuities. *Geochemistry, Geophysics, Geosystems*, *12*, Q08014. https://doi.org/10.1029/2011GC003668

Schmandt, B., Dueker, K. G., Humphreys, E. D., & Hansen, S. (2012). Hot mantle upwelling across the 660 beneath Yellowstone. *Earth and Planetary Science Letters*, *331-332*, 224–236. https://doi.org/10.1016/j.epsl.2012.03.025

Schmandt, B., Jacobsen, S. D., Becker, T. W., Liu, Z., & Dueker, K. G. (2014). Dehydration melting at the top of the lower mantle. *Science*, *344*(6189), 1265–1268.

Schmandt, B., & Lin, F. c. (2014). *P* and *S* wave tomography of the mantle beneath the United States. *Geophysical Research Letters*, *41*, 6342–6349. https://doi.org/10.1002/2014GL061231

Shearer, P. (2000). Upper mantle seismic discontinuities, *Earth's Deep Interior: Mineral Physics and Tomography from the Atomic to Global Scale* (pp. 115–131). Washington, DC: American Geophysical Union. https://doi.org/10.1029/GM117p0115

Sigloch, K. (2012). Mantle provinces under North America from multifrequency *P* wave tomography. *Geochemistry, Geophysics, Geosystems*, *12*(2), Q02W08. https://doi.org/10.1029/2010GC003421

Sigloch, K., McQuarrie, N., & Nolet, G. (2008). Two-stage subduction history under North America inferred from multiple-frequency tomography. *Nature Geoscience*, *1*(7), 458–462. https://doi.org/10.1038/ngeo231

Sigloch, K., & Mihalynuk, M. G. (2013). Intra-oceanic subduction shaped the assembly of Cordilleran North America. *Nature*, *496*(7443), 50–56. https://doi.org/10.1038/nature12019

Simmons, N. A., & Gurrola, H. (2000). Multiple seismic discontinuities near the base of the transition zone in the Earth's mantle. *Nature*, *405*, 559–562. https://doi.org/10.1038/35014589

Stixrude, L., & Lithgow-Bertelloni, C. (2011). Thermodynamics of mantle minerals—II. Phase equilibria. *Geophysical Journal International*, *184*(3), 1180–1213. https://doi.org/10.1111/j.1365-246X.2010.04890.x

Tauzin, B., Kim, S., & Afonso, J. C. (2018). Multiple phase changes in the mantle transition zone beneath northeast Asia: Constraints from teleseismic reflected and converted body-waves. *Journal of Geophysical Research: Solid Earth*, *123*. https://doi.org/10.1029/2017JB015238

Tauzin, B., Van Der Hilst, R. D., Wittlinger, G., & Ricard, Y. (2013). Multiple transition zone seismic discontinuities and low velocity layers below Western United States. *Journal of Geophysical Research: Solid Earth*, *118*, 2307–2322. https://doi.org/10.1002/jgrb.50182

van der Lee, S., & Nolet, G. (1997). Seismic image of the subducted trailing fragments of the Farallon plate. *Nature*, *386*(6622), 266–269. https://doi.org/10.1038/386266a0

Vinnik, L. (1977). Detection of waves converted from *P* to *SV* in the mantle. *Physics of the Earth and Planetary Interiors*, *15*(1), 39–45. https://doi.org/10.1016/0031-9201(77)90008-5

Wang, H., Gurnis, M., & Skogseid, J. (2017). Rapid Cenozoic subsidence in the Gulf of Mexico resulting from Hess rise conjugate subduction. *Geophysical Research Letters*, *44*, 10,930–10,938. https://doi.org/10.1002/2017GL074959

Wang, X., & Niu, F. (2011). Imaging the mantle transition zone beneath eastern and central China with CEArray receiver functions. *Earthquake Science*, *24*(1), 65–75. https://doi.org/10.1007/s11589-011-0770-x

Waszek, L., Schmerr, N. C., & Ballmer, M. D. (2018). Global observations of reflectors in the mid-mantle with implications for mantle structure and dynamics. *Nature Communications*, *9*(1), 385. https://doi.org/10.1038/s41467-017-02709-4

Workman, R. K., & Hart, S. R. (2005). Major and trace element composition of the depleted MORB mantle (DMM). *Earth and Planetary Science Letters*, *231*(1-2), 53–72. https://doi.org/10.1016/j.epsl.2004.12.005

Xie, S., & Tackley, P. J. (2004). Evolution of helium and argon isotopes in a convecting mantle. *Physics of the Earth and Planetary Interiors*, *146*(3-4), 417–439. https://doi.org/10.1016/j.pepi.2004.04.003

Xu, W., Lithgow-Bertelloni, C., Stixrude, L., & Ritsema, J. (2008). The effect of bulk composition and temperature on mantle seismic structure. *Earth and Planetary Science Letters*, *275*(1-2), 70–79. https://doi.org/10.1016/j.epsl.2008.08.012